

Phase-Separated Mo–Ni Alloy for Hydrogen Oxidation and Evolution Reactions with High Activity and Enhanced Stability

Jidong Song, Yan Qi Jin, Lei Zhang, Pengyu Dong, Jiawang Li, Fangyan Xie, Hao Zhang, Jian Chen, Yanshuo Jin,* Hui Meng,* and Xueliang Sun*

The development of alkaline polymer electrolyte fuel cells and alkaline water electrolysis requires nonprecious metal catalysts for the hydrogen oxidation reaction (HOR) and hydrogen evolution reaction (HER). Herein, it is reported a phase-separated Mo–Ni alloy (PS-MoNi) that is composed of Mo metal and embedded Ni metal nanoparticles. The PS-MoNi shows excellent hydrogen electrode activity with a high exchange current density ($-4.883 \text{ mA cm}^{-2}$), which is comparable to the reported highest value for non-noble catalysts. Moreover, the amorphous phase-separated Mo–Ni alloy has better structural and electrochemical stability than the intermetallic compound Mo–Ni alloy (IC-MoNi). The breakdown potential of PS-MoNi is as high as 0.32 V, which is much higher than that of reported IC-MoNi. The X-ray absorption near edge structure (XANES) and density functional theory (DFT) calculations indicate the electrons transfer from Mo to Ni for PS-MoNi, leading to suitable adsorption free energies of H^* (ΔG_{H^*}) on the surface of Mo. This means that the electron density modulation of Mo metal by embedded Ni metal nanoparticles can produce excellent HOR and HER performance.

advantage of alkaline polymer electrolyte fuel cells (APEFCs) and alkaline water electrolysis (AWE) is the use of nonprecious metal catalysts, which is expected to significantly reduce the cost and promote the practical application of hydrogen energy.^[6–8] At present, major obstacles to the application of APEFC and AWE are the slow kinetics of hydrogen electrode reactions and oxygen electrode reactions.^[9,10] Hydrogen oxidation reaction (HOR) and hydrogen evolution reaction (HER) belong to hydrogen electrode reactions, and Mo–Ni alloy is one of the most promising electrocatalysts for hydrogen electrode reactions.^[11–13] Intermetallic compound Mo–Ni alloy (IC-MoNi), such as MoNi_4 , MoNi_3 , and MoNi , will produce a synergistic effect between Mo and Ni for enhanced hydrogen electrode reactions.^[14–17] However, since the Mo element in IC-MoNi is unstable during the electro-

Hydrogen energy economy is one of the important ways to improve the use of clean and renewable energy, and has important economic and environmental significance.^[1–5] The

trode reaction process, the breakdown potential of IC-MoNi is low, resulting in poor electrochemical stability.^[14–17] Moreover, Ni also suffers from low stability at potentials about 0.1 V versus reversible hydrogen electrode (RHE) due to its relatively strong binding affinity toward oxygen species.^[18] How to improve the stability of IC-MoNi has become an important challenge.


The phase-separated alloy is different from the intermetallic compound alloy. For example, the phase-separated Mo–Ni alloy (PS-MoNi) is composed of phase-separated Mo metal phase and phase-separated Ni metal phase. Because Mo metal phase is stable and has a high breakdown potential,^[17] the PS-MoNi may have better structural and electrochemical stability than IC-MoNi. For PS-MoNi, the electron density of Mo metal can also be adjusted by Ni metal, which is similar to IC-MoNi.^[14–22] In addition, amorphous materials are more resistant to corrosion due to the absence of grain boundaries. Therefore, amorphous PS-MoNi may be a good material for HOR and HER with high activity and enhanced stability.

Herein, we synthesized the PS-MoNi composed of phase-separated Mo and Ni metal phases. The X-ray absorption spectroscopy (XAS) and the energy dispersive X-ray spectroscopy (EDS) mappings illustrate that we have synthesized PS-MoNi composed of Mo metal and embedded Ni metal nanoparticles. Excitingly, PS-MoNi shows excellent hydrogen electrode activity with the high exchange current density ($-4.883 \text{ mA cm}^{-2}$), which is comparable to the reported highest value for non-noble

J. Song, Y. Q. Jin, P. Dong, J. Li, Prof. Y. Jin, Prof. H. Meng
Guangdong Provincial Key Laboratory of Optical Fiber Sensing and Communications
Siyuan Laboratory
Guangzhou Key Laboratory of Vacuum Coating Technologies and New Energy Materials
Guangdong Provincial Engineering Technology Research Center of Vacuum Coating Technologies and New Energy Materials
Department of Physics
Jinan University
Guangzhou, Guangdong 510632, P. R. China
E-mail: jinyanshuo@email.jnu.edu.cn; tmh@jnu.edu.cn

Dr. L. Zhang, Prof. X. Sun
Department of Mechanical and Materials Engineering
University of Western Ontario
London, Ontario N6A 5B9, Canada
E-mail: xsun9@uwo.ca

Prof. F. Xie, H. Zhang, Prof. J. Chen
Instrumental Analysis & Research Center
Sun Yat-sen University
Guangzhou, Guangdong 510275, P. R. China

 The ORCID identification number(s) for the author(s) of this article can be found under <https://doi.org/10.1002/aenm.202003511>.

DOI: 10.1002/aenm.202003511

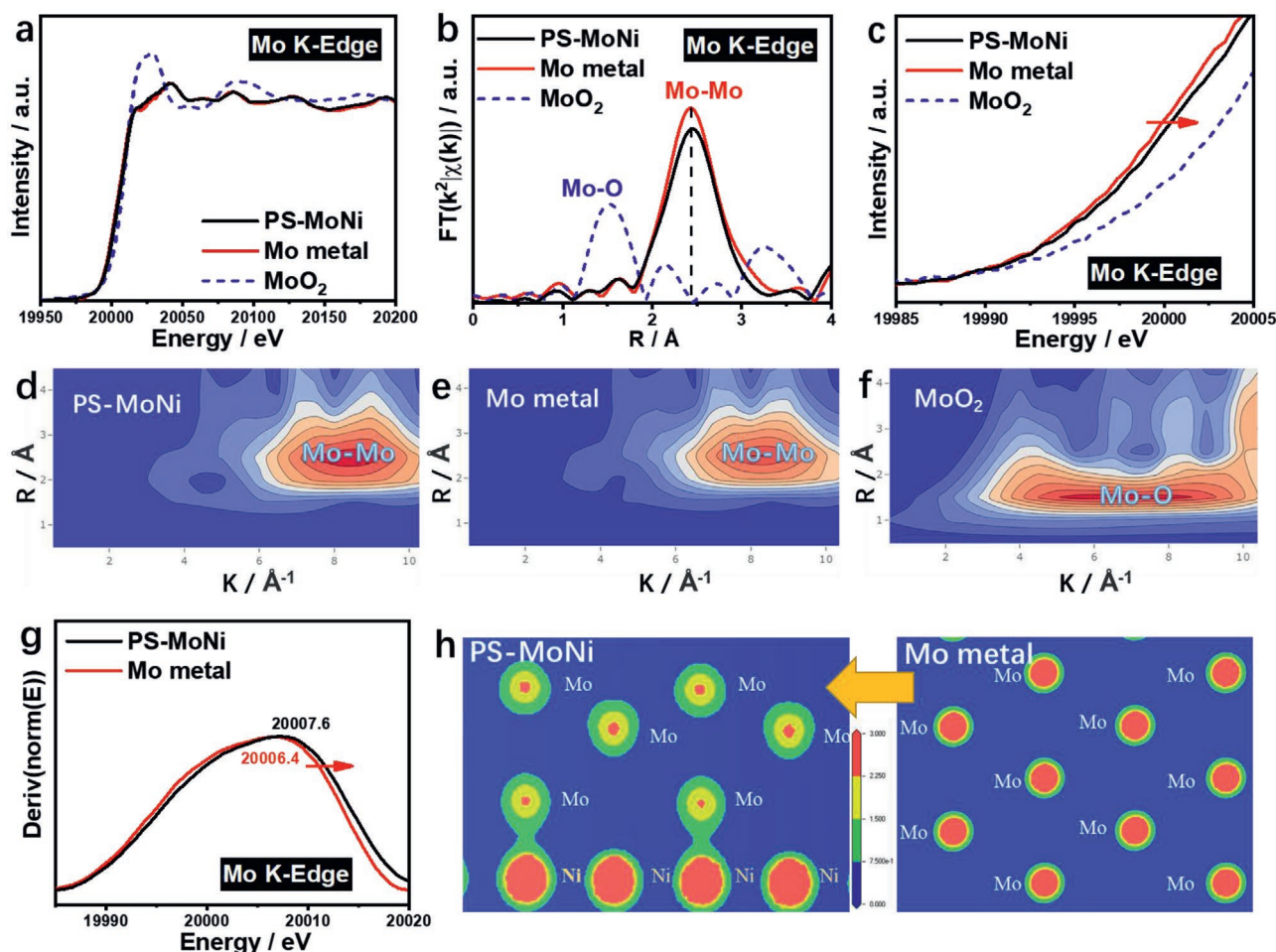


Figure 1. a) Mo *K*-edge XAS of PS-MoNi obtained using Mo metal and MoO₂ as references. b) The corresponding *k*²-weighted FT of EXAFS spectra at Mo *K*-edge in the *R* spacing of PS-MoNi, Mo metal, and MoO₂. c) Mo *K*-edge XANES spectra of PS-MoNi, Mo metal, and MoO₂. d–f) Wavelet transforms for the *k*²-weighted EXAFS signals at Mo *K*-edge of PS-MoNi, Mo metal, and MoO₂. g) The first derivative of XANES at Mo *K*-edge of PS-MoNi and Mo metal. h) The electron density PS-MoNi and Mo metal.

catalysts. Moreover, PS-MoNi shows excellent HOR activity in a large overpotential window of 0–0.32 V versus RHE, which is more resistant to electrochemical oxidation than IC-MoNi. X-ray absorption near edge structure (XANES) and density functional theory (DFT) calculations indicate the electron transfer from Mo to Ni. DFT calculations reveal that the electron deficiency on Mo enhances the catalytic performance for reversible HER and HOR by optimizing the ΔG_{H^*} of Mo.

PS-MoNi was synthesized on nickel foam by the hydrothermal method and then the heat-treatment method at 450 °C for 1 h in H₂ atmosphere. IC-MoNi was synthesized in the same way, but with a different concentration of solutions (Figure S1, Supporting Information). XAS was usually used to characterize the structure of amorphous materials. The experiment data and simulation data of the corresponding *k*²-weighted Fourier transform (FT) of extended X-ray absorption fine structure (EXAFS) spectra at Mo *K*-edge in the *R* spacing of PS-MoNi are shown in Figure S2 (Supporting Information). As shown in Figure 1a, the XAS spectrum at Mo *K*-edge of PS-MoNi is basically consistent with that of Mo metal, and is different from MoO₂. EXAFS is a powerful tool to study

the amorphous structure.^[22] As shown in Figure 1b, for Mo metal, the bond length of ≈ 2.4 Å at Mo *K*-edge in the *R* spacing belongs to Mo–Mo bond. For MoO₂, the bond length of ≈ 1.5 Å at Mo *K*-edge in the *R* spacing belongs to Mo–O bond. The corresponding *k*²-weighted FT of EXAFS spectrum at Mo *K*-edge in the *R* spacing of PS-MoNi is also basically the same as that of Mo metal and different from that of MoO₂. Therefore, we infer that the Mo element in PS-MoNi exists as phase-separated Mo metal. To confirm the electron transfer in the PS-MoNi, XANES spectra at Mo *K*-edge of PS-MoNi, Mo metal, and MoO₂ were recorded. Figure 1c shows that the XANES spectrum at Mo *K*-edge of PS-MoNi moves to a higher binding energy position compared with Mo metal. This means that the phase-separated Mo metal loses electrons in the PS-MoNi.

In the wavelet transform spectrum, the horizontal axis shows the wave vector number *k*, which is the key to distinguish different kinds of coordination atoms.^[23] As shown in Figure 1d–f, the coordination features of Mo in PS-MoNi are similar to those in Mo metal, with an intensity maximum at ≈ 2.4 Å and in the high-*k* part assigned to Mo–Mo coordination. For MoO₂, the high-intensity region was observed at ≈ 1.5 Å and

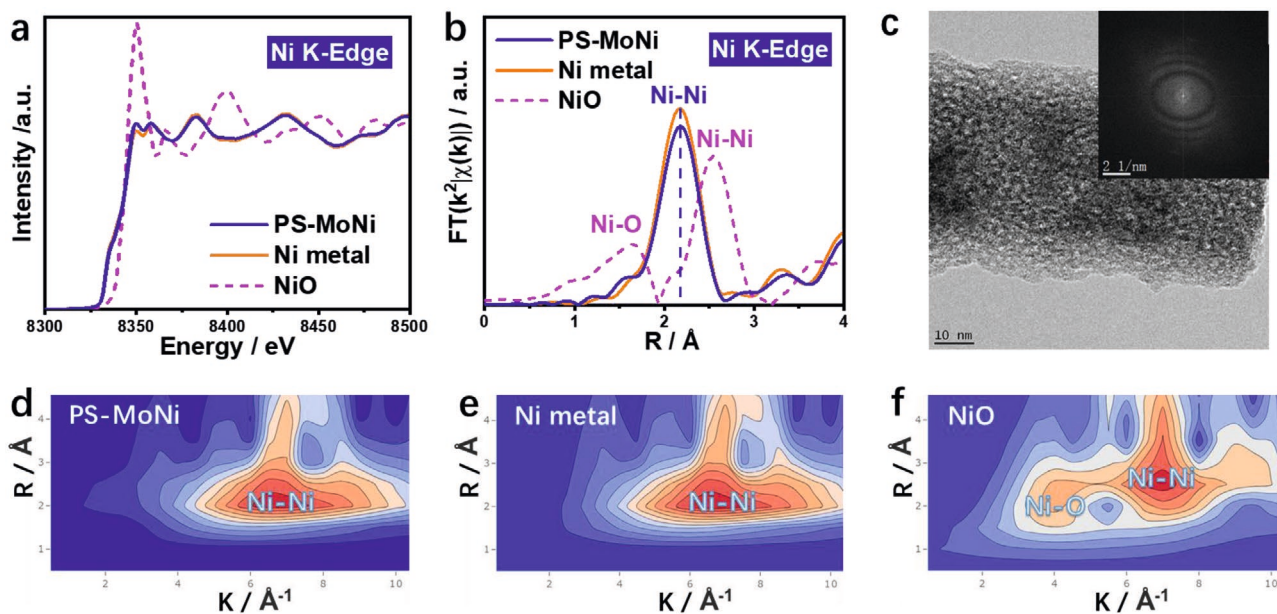


Figure 2. a) Ni *K*-edge XAS of PS-MoNi obtained using Ni metal and NiO as references. b) The corresponding k^2 -weighted FT of EXAFS spectra at Ni *K*-edge in the *R* spacing of PS-MoNi, Ni metal, and NiO. c) The HRTEM and FFT patterns of the corresponding plane of PS-MoNi. d–f) Wavelet transforms for the k^2 -weighted EXAFS signals at Ni *K*-edge of PS-MoNi, Ni metal, and NiO.

in the low-*k* part assigned to Mo–O coordination. An atom with a small atomic number has a weak scattering ability for photoelectrons, and its high-intensity region will appear in the low-*k* part. An atom with a large atomic number is just the opposite, and its intensity maximum will appear in the high-*k* part. In order to accurately analyze the electron density of Mo in the PS-MoNi, the first derivatives of XANES at Mo *K*-edge of PS-MoNi and Mo metal were recorded. As shown in Figure 1g, the maximum value at Mo *K*-edge of amorphous PS-MoNi (20 007.6 eV) is bigger than that of Mo (20 006.4 eV). This means that the Mo element loses electrons in the PS-MoNi. The electron transfer from Mo metal to the embedded Ni metal nanoparticles is the key to the unique electronic structure and properties of PS-MoNi, which are obviously different from those of pure Mo metal.

According to previous literature, amorphous modeling is very difficult, so crystalline modeling is used to simplify calculations.^[24–27] To study the electron density modulation of amorphous Mo metal by embedded Ni metal nanoparticles, crystalline structures are used to model them. The optimized models of Mo metal (Figure S3, Supporting Information), Ni metal (Figure S4, Supporting Information), and PS-MoNi (Figure S5, Supporting Information) were established in order to calculate their electron density. Comparing the electron density of PS-MoNi (Figure 1h, left) and the electron density of Mo metal (Figure 1h, right), we can observe that the electrons of Mo were transferred to Ni in PS-MoNi, which is consistent with the conclusions that we got from our experiments. In order to reveal the nature of electron transfer more scientifically, we introduced the electronegativity of the elements for comparison. We know that the element electronegativity reveals its ability to gain or lose electrons. The comparison of the electronegativity of some transition-metal elements is shown in Table S1 (Supporting Information). The electronegativity of element Mo

is smaller than that of element Ni, which means that when Mo and Ni metals are combined, Ni is more likely to attract electrons and cause electron transfer.

The XAS spectrum at Ni *K*-edge of PS-MoNi (Figure 2a) is basically consistent with that of the Ni metal, and is different from NiO. The corresponding k^2 -weighted FT of EXAFS spectra at Ni *K*-edge in the *R* spacing of PS-MoNi, Ni metal, and NiO are shown in Figure 2b. For Ni metal, the bond length of ≈ 2.2 Å at Ni *K*-edge in the *R* spacing belongs to Ni–Ni bond. For NiO, the bond lengths of ≈ 1.7 and ≈ 2.6 Å at Ni *K*-edge in the *R* spacing belong to Ni–O and Ni–Ni bonds, respectively. The corresponding k^2 -weighted FT of EXAFS spectrum at Ni *K*-edge in the *R* spacing of PS-MoNi is also basically the same as that of Ni metal and different from that of NiO. Therefore, we infer that the Ni element in PS-MoNi exists as Ni metal. Figure S6 (Supporting Information) further shows the different metal-to-metal bond lengths for Mo (≈ 2.4 Å) and Ni (≈ 2.2 Å) in PS-MoNi, which means that Mo and Ni elements in PS-MoNi exist as Mo and Ni metals, respectively. To demonstrate the morphologies and structures of the PS-MoNi, scanning electron microscopy (SEM) images of PS-MoNi are shown in Figure S7 (Supporting Information), and transmission electron microscopy (TEM) images of amorphous PS-MoNi are shown in Figure S8 (Supporting Information). The TEM images clarify the difference of structures between PS-MoNi (Figure S8, Supporting Information) and IC-MoNi (Figure S9, Supporting Information). The high resolution transmission electron microscopy (HRTEM) and fast Fourier transform (FFT) patterns of the corresponding planes are shown in Figure 2c, which shows that it is an amorphous structure. Furthermore, the EDS mappings (Figures S10 and S11, Supporting Information) and the corresponding EDS spectra (Figure S12, Supporting Information) demonstrate the uniform distribution of Ni nanoparticles (mass percent $\approx 18\%$) at the nanoscale in PS-MoNi. In addition, Figure 2d–f shows that the

coordination features of Ni in PS-MoNi are similar to those in Ni metal, with an intensity maximum at $\approx 2.2 \text{ \AA}$ and in the high- k part assigned to Ni–Ni coordination. For NiO, one high-intensity region was observed at $\approx 1.7 \text{ \AA}$ and in the low- k part assigned to Ni–O coordination, and the other high-intensity region was observed at $\approx 2.6 \text{ \AA}$ and in the high- k part assigned to Ni–Ni coordination. The above experimental results illustrate that we have synthesized amorphous Mo metal with embedded Ni metal nanoparticles (PS-MoNi). Figure S13a,b (Supporting Information) demonstrates the schematic diagrams of PS-MoNi and IC-MoNi alloys to distinguish them. Figure S13c (Supporting Information) shows the corresponding k^2 -weighted FT of EXAFS spectra at Mo K -edge in the R spacing of PS-MoNi and Mo metal, compared with IC-MoNi, which further explains the difference between PS-MoNi and IC-MoNi.^[16] To further confirm the electron transfer in the PS-MoNi, Figure S14 (Supporting Information) demonstrates that the maximum value at Ni K -edge of PS-MoNi (8332.8 eV) is smaller than Ni (8333.1 eV). It means the Ni in PS-MoNi obtains electrons. These analyses further indicate that the electrons from amorphous Mo metal are transferred to embedded Ni metal nanoparticles in PS-MoNi. Comparing the electron density of PS-MoNi (Figure S15, left, Supporting Information) and the electron density of Ni metal (Figure S1, right, Supporting Information), we can observe that embedded Ni metal nanoparticles obtain electrons in PS-MoNi, which is consistent with the conclusions that we got from our experiments.

A widely accepted cognition in hydrogen electrochemistry is that a high catalytic performance is anticipated if ΔG_{H^*} is close to 0 eV.^[6,12,24,25] Therefore, hydrogen adsorptions on Mo metal

(Figure S16, Supporting Information), Ni metal (Figure S17, Supporting Information), and PS-MoNi (Figure 3a; Figure S18, Supporting Information) were also investigated by DFT calculations. Because amorphous modeling is very difficult, crystalline modeling is used to simplify calculations.^[25–28] Figure 3b describes the ΔG_{H^*} on Mo and Ni sites in PS-MoNi compared with Mo and Ni metals. Since the electrons of Mo were transferred to Ni in PS-MoNi, the ΔG_{H^*} of Mo site in PS-MoNi was increased to -0.13 eV , very close to the Pt of -0.09 eV , which leads to the excellent electrocatalytic performance in hydrogen electrochemistry.

Figure 3c exhibits the polarization curves of the PS-MoNi@nickel foam (NF), IC-MoNi@NF, Ni@NF (Figures S19 and S20, Supporting Information), NF, and Pt/C for HER in 1 M KOH solution. The PS-MoNi@NF exhibited extraordinary HER activity and required an overpotential of only 30 mV to deliver a current density of -10 mA cm^{-2} , which is comparable to excellent non-noble catalysts (Table S2, Supporting Information).^[20,29–40] It also can be found the activity in HER of the PS-MoNi@NF is far superior to the IC-MoNi@NF, which requires an overpotential of nearly 76 mV to achieve the current density of -10 mA cm^{-2} . To investigate the HER kinetics, the Tafel slope was calculated in Figure S21 (Supporting Information). It can be found that PS-MoNi@NF electrode shows a low Tafel slope of 37 mV dec^{-1} , which means that the decrease in charge-transfer resistance during the HER process accelerates HER kinetics.^[41–43] We compare the Tafel slopes of PS-MoNi@NF and IC-MoNi@NF, and it shows that the PS-MoNi@NF has a stronger response power than IC-MoNi@NF and reveals the reason why PS-MoNi@NF has the better performance for HER. Figure S22 (Supporting Information) shows the electrochemical

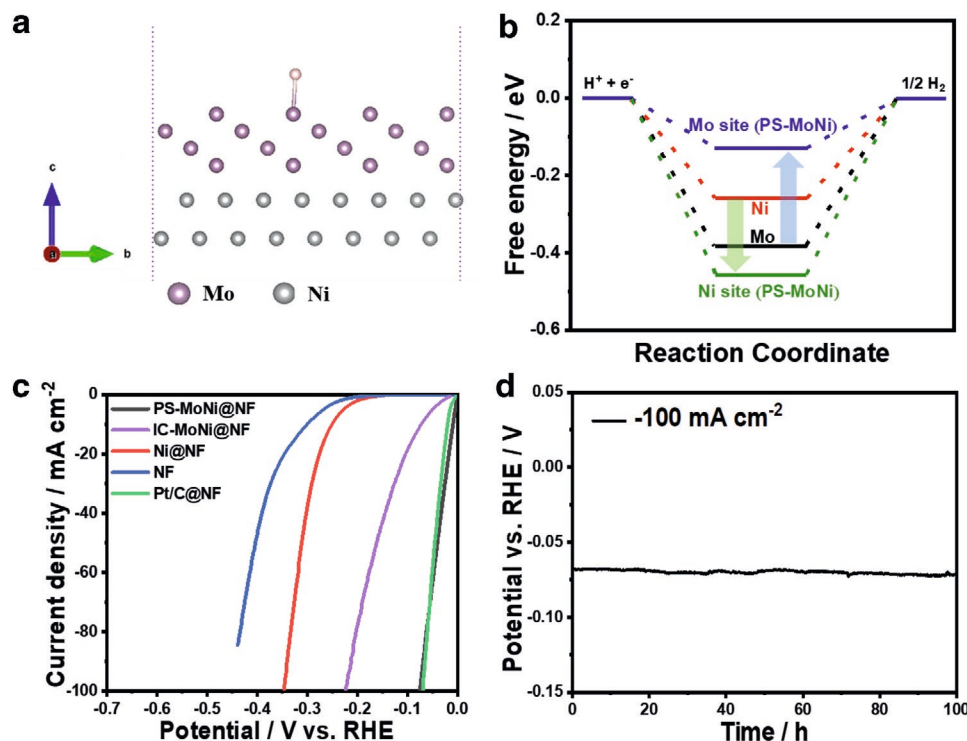


Figure 3. a) Optimized models of PS-MoNi. b) Hydrogen adsorption free energy (ΔG_{H^*}) on the Mo metal, Ni metal, and PS-MoNi. c) LSV curves of PS-MoNi@NF, IC-MoNi@NF, Ni@NF, NF, and Pt/C@NF for HER were tested in 1 M KOH solution at 25 °C with a scan rate of 1 mV s^{-1} . d) Chronoamperometry curve of PS-MoNi@NF for HER at a constant current density of -100 mA cm^{-2} in 1 M KOH.

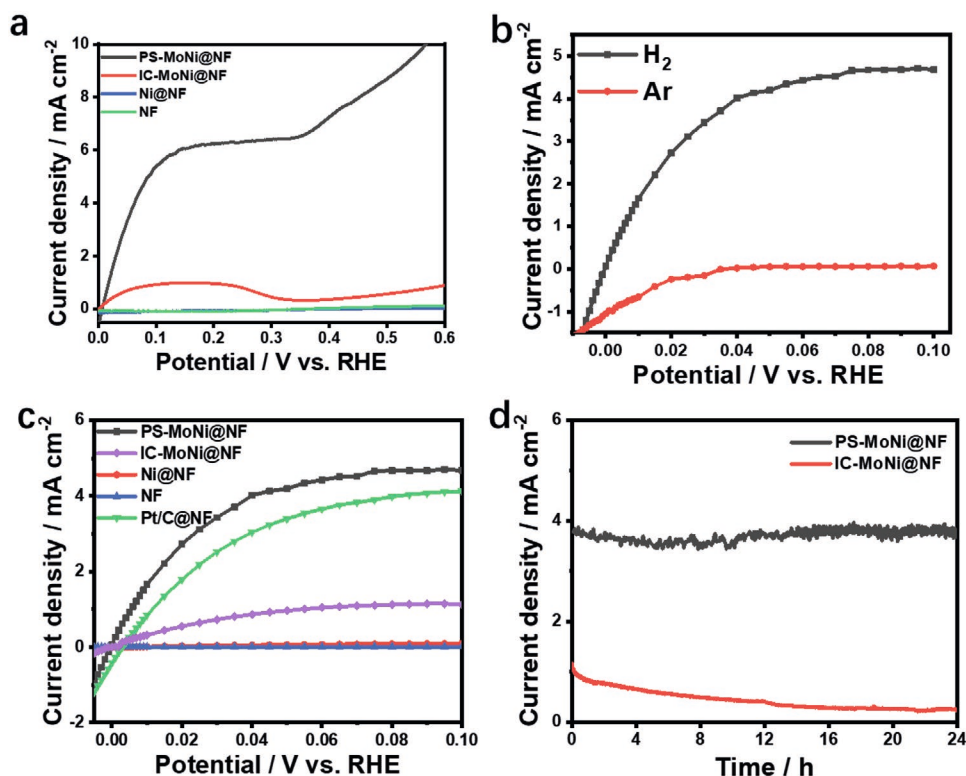


Figure 4. a) LSV curves of PS-MoNi@NF, IC-MoNi@NF, Ni@NF, and NF were tested from 0 to 0.6 V versus RHE in 0.1 M KOH solution at 25 °C with a scan rate of 1 mV s⁻¹. b) The steady-state polarization curves of PS-MoNi@NF collected in H₂-saturated and Ar-saturated 0.1 M KOH, respectively. c) The steady-state polarization curves of PS-MoNi@NF, IC-MoNi@NF, Ni@NF, NF, and Pt/C@NF collected in H₂-saturated 0.1 M KOH solution. d) Chronopotentiometric curve of PS-MoNi@NF and IC-MoNi@NF for HOR at a constant potential of 0.1 V.

impedance spectroscopy Nyquist plots of PS-MoNi@NF, IC-MoNi@NF, Ni@NF, and NF, which also reveal that PS-MoNi@NF has faster reaction kinetics in electrochemical reactions. For catalysts with excellent performance, stability during the reaction is indispensable. The chronopotentiometry curve of PS-MoNi@NF shows outstanding stability for HER at the current densities of -10 mA cm^{-2} (Figure S23, Supporting Information) and -100 mA cm^{-2} (Figure 3d). We also characterized the TEM images of the samples after the electrochemical stability test in Figure S24 (Supporting Information). It can be seen that the structure is basically unchanged compared to the sample before the stability test, which further proves that the PS-MoNi has excellent stability.

Linear sweep voltammetry (LSV) curve of PS-MoNi@NF, IC-MoNi@NF, Ni@NF, and NF (Figure 4a) were tested from 0 to 0.6 V versus RHE in 0.1 M KOH solution. Excitingly, PS-MoNi@NF shows excellent activity in a large potential window of 0–0.32 V versus RHE due to the reactive Mo sites in PS-MoNi, which is more resistant to electrochemical oxidation than Mo–Ni intermetallic compound or Ni metal.^[14–17] Therefore, the only possibility is that the active site of PS-MoNi is Mo site, which is in good agreement with the previous experimental results and theoretical calculations. To test the stability of PS-MoNi@NF in reversible HER/HOR, the LSV curve of PS-MoNi@NF from -0.05 to 0.1 V versus RHE in 0.1 M KOH solution at 25 °C with a scan rate of 1 mV s⁻¹ before and after stability testing was recorded in Figure S25 (Supporting Information). Excitingly, PS-MoNi@NF shows excellent stability in reversible HER/HOR.

Figure 4b compares the steady-state polarization curves of PS-MoNi@NF collected in H₂-saturated (Figure S26, Supporting Information) and Ar-saturated 0.1 M KOH solutions, respectively. The apparent anodic current at positive potential versus RHE was obtained in the H₂-saturated solution, which indicates that HOR takes place on PS-MoNi@NF. As plotted in Figure 4c, the HOR catalytic current density of PS-MoNi@NF takes off at 0 V versus RHE and is very close to that on Pt/C@NF in the potential window of 0–0.1 V versus RHE. Compared with IC-MoNi@NF, the PS-MoNi@NF collected the larger current density signal at each corresponding potential. In addition, PS-MoNi@NF shows the excellent performance in both H₂-saturated 1 and 0.1 M KOH solutions (Figure S27, Supporting Information).

To compare the intrinsic activity, the exchange current density was estimated based on the electric window region from -10 to 10 mV versus RHE.^[44–46] Figure S25 (Supporting Information) shows the *i*-*t* curve at each different voltage of PS-MoNi@NF. Figure S28 and Table S3 (Supporting Information) show that the exchange current density of PS-MoNi@NF (4.883 mA cm^{-2}) is 1.35 times higher than that of Pt/C@NF (3.615 mA cm^{-2}) and 5.27 times higher than that of IC-MoNi@NF (0.916 mA cm^{-2}), which are comparable to excellent non-noble catalysts.^[6,12,27,47–49] To further investigate the stability of PS-MoNi@NF and IC-MoNi@NF, the chronoamperometry at 0.1 V versus RHE (Figure 4d) shows the stable current density. With the passage of the test time, the performance of the IC-MoNi@NF has

been significantly attenuated, while the performance of the PS-MoNi@NF is still stable.

In summary, we successfully synthesized the low-cost PS-MoNi electrocatalyst for enhanced HOR and HER. Through tuning ΔG_{H^*} on Mo sites, PS-MoNi shows excellent activity with the high exchange current density ($-4.883 \text{ mA cm}^{-2}$), which is comparable to the reported highest value for non-noble catalysts. In comparison with the IC-MoNi, the PS-MoNi shows both excellent activity and enhanced stability for HER and HOR. Because the active site is Mo site, the breakdown potential of PS-MoNi is as high as 0.32 V, which is more resistant to electrochemical oxidation than IC-MoNi or Ni metal. This means that a PS-MoNi can enhance the power output and application potential of APEFC. Our work provides a facile strategy for designing competent catalysts for HOR and HER.

Supporting Information

Supporting Information is available from the Wiley Online Library or from the author.

Acknowledgements

J.S. and Y.Q. contributed equally to this work. This work was supported by the National Natural Science Foundation of China (Grant Nos. 21576301, 22075102, and 22005120), the Natural Science Foundation of Guangdong Province, China (Grant No. 2017A030313048), and the Fundamental Research Funds for the Central Universities (Grant No. 21619317).

Conflict of Interest

The authors declare no conflict of interest.

Data Availability Statement

Research data are not shared.

Keywords

breakdown potential, hydrogen evolution reaction, hydrogen oxidation reaction, nonprecious metals, phase-separated alloys

Received: November 7, 2020

Revised: January 15, 2021

Published online:

- [1] Y. Zhou, Z. Xie, J. Jiang, J. Wang, X. Song, Q. He, W. Ding, Z. Wei, *Nat. Catal.* **2020**, *3*, 454.
- [2] M. K. Debe, *Nature* **2012**, *486*, 43.
- [3] P. Ganguly, M. Harb, Z. Cao, L. Cavallo, A. Breen, S. Dervin, D. D. Dionysiou, S. C. Pillai, *ACS Energy Lett.* **2019**, *4*, 1687.
- [4] X. Wang, C. Xu, M. Jaroniec, Y. Zheng, S. Z. Qiao, *Nat. Commun.* **2019**, *10*, 4876.
- [5] H. Jin, X. Liu, A. Vasileff, Y. Jiao, Y. Zhao, Y. Zheng, S. Z. Qiao, *ACS Nano* **2018**, *12*, 12761.
- [6] F. Song, W. Li, J. Yang, G. Han, P. Liao, Y. Sun, *Nat. Commun.* **2018**, *9*, 4531.
- [7] T. Kou, M. Chen, F. Wu, T. J. Smart, S. Wang, Y. Wu, Y. Zhang, S. Li, S. Lall, Z. Zhang, Y. S. Liu, J. Guo, G. Wang, Y. Ping, Y. Li, *Nat. Commun.* **2020**, *11*, 590.
- [8] H. Jin, Q. Gu, B. Chen, C. Tang, Y. Zheng, H. Zhang, M. Jaroniec, S. Z. Qiao, *Chem* **2020**, *6*, 2382.
- [9] H. Jin, X. Liu, S. Chen, A. Vasileff, L. Li, Y. Jiao, L. Song, Y. Zheng, S. Z. Qiao, *ACS Energy Lett.* **2019**, *4*, 805.
- [10] X. Wang, T. Ouyang, L. Wang, J. Zhong, T. Ma, Z. Liu, *Angew. Chem.* **2019**, *131*, 13425.
- [11] F. Yang, X. Bao, Y. Zhao, X. Wang, G. Cheng, W. Luo, *J. Mater. Chem. A* **2019**, *7*, 10936.
- [12] F. Yang, X. Bao, P. Li, X. Wang, G. Cheng, S. Chen, W. Luo, *Angew. Chem.* **2019**, *131*, 14317.
- [13] H. Zeng, S. Chen, Y. Q. Jin, J. Li, J. Song, Z. Le, G. Liang, H. Zhang, F. Xie, J. Chen, Y. Jin, X. Chen, H. Meng, *ACS Energy Lett.* **2020**, *5*, 1908.
- [14] J. H. J. Wijten, R. L. Riemersma, J. Gauthier, L. D. B. Mandemaker, M. W. G. M. (Tiny) Verhoeven, J. P. Hofmann, K. Chan, B. M. Weckhuysen, *ChemSusChem* **2019**, *12*, 3491.
- [15] S. Kabir, K. Lemire, K. Artyushkova, A. Roy, M. Odgaard, D. Schlueter, A. Oshchepkov, A. Bonnefont, E. Savinova, D. C. Sabarirajan, P. Mandal, E. J. Crumlin, I. V. Zhenyuk, P. Atanassov, A. Serov, *J. Mater. Chem. A* **2017**, *5*, 24433.
- [16] Y. Duan, Z. Y. Yu, L. Yang, L. R. Zheng, C. T. Zhang, X. T. Yang, F. Y. Gao, X. L. Zhang, X. Yu, R. Liu, H. H. Ding, C. Gu, X. S. Zheng, L. Shi, J. Jiang, J. F. Zhu, M. R. Gao, S. H. Yu, *Nat. Commun.* **2020**, *11*, 4789.
- [17] C. R. Lee, S. G. Kang, *J. Power Sources* **2000**, *87*, 64.
- [18] W. Ni, A. Krammer, C. S. Hsu, H. M. Chen, A. Schüller, X. Hu, *Angew. Chem., Int. Ed.* **2019**, *58*, 7445.
- [19] J. K. Nørskov, T. Bligaard, A. Logadottir, J. R. Kitchin, J. G. Chen, S. Pandalov, U. Stimming, *J. Electrochem. Soc.* **2005**, *152*, J23.
- [20] J. Duan, S. Chen, C. A. Ortíz-Ledón, M. Jaroniec, S. Z. Qiao, *Angew. Chem., Int. Ed.* **2020**, *59*, 8181.
- [21] L. Wu, N. Y. Dzade, M. Yu, B. Mezari, A. J. F. Van Hoof, H. Friedrich, N. H. De Leeuw, E. J. M. Hensen, J. P. Hofmann, *ACS Energy Lett.* **2019**, *4*, 1733.
- [22] G. Wu, X. Zheng, P. Cui, H. Jiang, X. Wang, Y. Qu, W. Chen, Y. Lin, H. Li, X. Han, Y. Hu, P. Liu, Q. Zhang, J. Ge, Y. Yao, R. Sun, Y. Wu, L. Gu, X. Hong, Y. Li, *Nat. Commun.* **2019**, *10*, 4855.
- [23] Z. Xia, H. Zhang, K. Shen, Y. Qu, Z. Jiang, *Phys. B* **2018**, *542*, 12.
- [24] B. Zhang, X. Zheng, O. Voznyy, R. Comin, M. Bajdich, M. García-Melchor, L. Han, J. Xu, M. Liu, L. Zheng, F. P. G. De Arquer, C. T. Dinh, F. Fan, M. Yuan, E. Yassitepe, N. Chen, T. Regier, P. Liu, Y. Li, P. De Luna, A. Janmohamed, H. L. Xin, H. Yang, A. Vojvodic, E. H. Sargent, *Science* **2016**, *352*, 333.
- [25] X. Wang, Y. Zheng, W. Sheng, Z. J. Xu, M. Jaroniec, S. Z. Qiao, *Mater. Today* **2020**, *36*, 125.
- [26] Y. Jin, S. Huang, X. Yue, H. Du, P. K. Shen, *ACS Catal.* **2018**, *8*, 2359.
- [27] J. Xu, C. Zhang, H. Liu, J. Sun, R. Xie, Y. Qiu, F. Lü, Y. Liu, L. Zhuo, X. Liu, J. Luo, *Nano Energy* **2020**, *70*, 104529.
- [28] F. Song, W. Li, J. Yang, G. Han, T. Yan, X. Liu, Y. Rao, P. Liao, Z. Cao, Y. Sun, *ACS Energy Lett.* **2019**, *4*, 1594.
- [29] R. Zhang, X. Ren, S. Hao, R. Ge, Z. Liu, A. M. Asiri, L. Chen, Q. Zhang, X. Sun, *J. Mater. Chem. A* **2018**, *6*, 1985.
- [30] S. Q. Liu, H. R. Wen, Y. W. Z. Ying-Guo, X. Z. Fu, R. Sun, C. P. Wong, *Nano Energy* **2018**, *44*, 7.
- [31] H. Jin, X. Liu, Y. Jiao, A. Vasileff, Y. Zheng, S. Z. Qiao, *Nano Energy* **2018**, *53*, 690.
- [32] Y. Zang, S. Niu, Y. Wu, X. Zheng, J. Cai, J. Ye, Y. Xie, Y. Liu, J. Zhou, J. Zhu, X. Liu, G. Wang, Y. Qian, *Nat. Commun.* **2019**, *10*, 1217.
- [33] Y. Liu, S. Liu, Y. Wang, Q. Zhang, L. Gu, S. Zhao, D. Xu, Y. Li, J. Bao, Z. Dai, *J. Am. Chem. Soc.* **2018**, *140*, 2731.
- [34] S. Deng, Y. Zhong, Y. Zeng, Y. Wang, Z. Yao, F. Yang, S. Lin, X. Wang, X. Lu, X. Xia, J. Tu, *Adv. Mater.* **2017**, *29*, 1700748.

- [35] Z. Chen, Y. Song, J. Cai, X. Zheng, D. Han, Y. Wu, Y. Zang, S. Niu, Y. Liu, J. Zhu, X. Liu, G. Wang, *Angew. Chem.* **2018**, *130*, 5170.
- [36] Q. Xu, Y. Liu, H. Jiang, Y. Hu, H. Liu, C. Li, *Adv. Energy Mater.* **2019**, *9*, 1802553.
- [37] L. An, J. Feng, Y. Zhang, R. Wang, H. Liu, G. C. Wang, F. Cheng, P. Xi, *Adv. Funct. Mater.* **2019**, *29*, 1805298.
- [38] Y. Wu, Y. Liu, G. D. Li, X. Zou, X. Lian, D. Wang, L. Sun, T. Asefa, X. Zou, *Nano Energy* **2017**, *35*, 161.
- [39] C. Zhu, A. L. Wang, W. Xiao, D. Chao, X. Zhang, N. H. Tiep, S. Chen, J. Kang, X. Wang, J. Ding, J. Wang, H. Zhang, H. J. Fan, *Adv. Mater.* **2018**, *30*, 1705516.
- [40] X. Peng, A. M. Qasim, W. Jin, L. Wang, L. Hu, Y. Miao, W. Li, Y. Li, Z. Liu, K. Huo, K. Yin Wong, P. K. Chu, *Nano Energy* **2018**, *53*, 66.
- [41] Y. Li, X. Tan, S. Chen, X. Bo, H. Ren, S. C. Smith, C. Zhao, *Angew. Chem., Int. Ed.* **2019**, *58*, 461.
- [42] C. Tang, R. Zhang, W. Lu, Z. Wang, D. Liu, S. Hao, G. Du, A. M. Asiri, X. Sun, *Angew. Chem., Int. Ed.* **2017**, *56*, 842.
- [43] Y. Li, H. Wang, L. Xie, Y. Liang, G. Hong, H. Dai, *J. Am. Chem. Soc.* **2011**, *133*, 7296.
- [44] J. Zheng, W. Sheng, Z. Zhuang, B. Xu, Y. Yan, *Sci. Adv.* **2016**, *2*, 1501602.
- [45] Y. Cong, B. Yi, Y. Song, *Nano Energy* **2018**, *44*, 288.
- [46] S. Lu, Z. Zhuang, *J. Am. Chem. Soc.* **2017**, *139*, 5156.
- [47] Y. Yang, X. Sun, G. Han, X. Liu, X. Zhang, Y. Sun, M. Zhang, Z. Cao, Y. Sun, *Angew. Chem.* **2019**, *131*, 10754.
- [48] T. Wang, M. Wang, H. Yang, M. Xu, C. Zuo, K. Feng, M. Xie, J. Deng, J. Zhong, W. Zhou, T. Cheng, Y. Li, *Energy Environ. Sci.* **2019**, *12*, 3522.
- [49] Z. Zhuang, S. A. Giles, J. Zheng, G. R. Jenness, S. Caratzoulas, D. G. Vlachos, Y. Yan, *Nat. Commun.* **2016**, *7*, 10141.